

## **NOWACKI'S DOUBLE SHEAR TEST IN THE FRAMEWORK OF THE ANISOTROPIC THERMO-ELASTO-VISCOPLASTIC MATERIAL MODEL<sup>1</sup>**

ADAM GLEMA  
TOMASZ ŁODYGOWSKI  
WOJCIECH SUMELKA

*Poznan University of Technology, Faculty of Civil and Environmental Engineering, Poznań, Poland  
e-mail: adam.glema@put.poznan.pl; tomasz.lodygowski@put.poznan.pl;  
wojciech.sumelka@put.poznan.pl*

*The paper is dedicated to the memory  
of Prof. Wojciech K. Nowacki*

In the paper, the numerical simulation of Nowacki's double shear test in the framework of recently proposed viscoplasticity theory for anisotropic solids is presented. The numerical analysis comprises the full spatial modelling and is carried out for the DH-36 steel sheet in adiabatic conditions (the analysis of anisotropic bodies can be led only on 3D models). During analyses, strain rates of order  $10^4$ - $10^7$  s<sup>-1</sup> are observed and the process time duration up to full damage (loss of continuity in the localisation zone) is around 150-300  $\mu$ s. The novelty of the research is focused on the formulation that includes the anisotropy of the intrinsic microdamage process. Thus, it makes possible to obtain qualitatively and quantitatively new results compared with the existing models, like tracing the softening directions and better (closer to experiment) prediction of damage paths.

*Key words:* microdamage anisotropy, metals, constitutive relation

### **1. Introduction**

Modern constitutive models need sophisticated experimental techniques for the identification of material functions and parameters assumed in the the-

---

<sup>1</sup>The support of the Polish Ministry of Science and Higher Education under grant NN519 419435 "The evolution of properties and failure criteria of materials and structures under fast dynamic loadings" is kindly acknowledged.

oretical description. To the most challenging tasks from the experimental and simultaneously the theoretical points of view, concerning the analysis of metals behaviour (the central point in this paper), belong to the investigation of strain, stress, temperature and softening fields up to full damage during extremely fast dynamic processes. Such experimental evidences include crucial properties like e.g., local strain rates of the order  $10^4$ - $10^7$  s<sup>-1</sup>, temperature rise in the strain localisation zones up to the melting point and anisotropy induced by evolving the intrinsically anisotropic microdamage process.

One of experimental techniques which allows for the analysis of the mentioned phenomena is the recently developed test for dynamic plane shearing of steel sheet (Gary and Nowacki, 1994; Klepaczko *et al.*, 1999) – which we call *Nowacki's double shear test* after the name of its inventor. The experimental set-up was broadly analysed both experimentally and theoretically (Klepaczko *et al.*, 1999; Nowak *et al.*, 2007; Pęcherski *et al.*, 2009). Nevertheless, we are going to present numerical calculations up to full material degradation in the specimen (loss of continuity in the softening zones) and, moreover, to include modelling of the intrinsic microdamage process as an anisotropic one. Notice, that the anisotropy of microdamage plays a crucial role in the proper description of damage, giving (as it will be discussed in the following sections) qualitatively and quantitatively new results compared with the existing models (Sumelka, 2009).

Thus, the fundamental aim of the paper concerns the numerical simulation of Nowacki's double shear test in the framework of viscoplasticity theory for anisotropic solids (Perzyna, 2008; Glema *et al.*, 2009; Sumelka, 2009).

Section 2 deals with the description of Nowacki's double shear test. The direct impact variation of this experimental technique is selected. The crucial results of this section state a base for proper numerical modelling presented in Section 4.

In Section 3, the fundamental results of viscoplasticity theory for anisotropic solids are presented. The discussion on a microdamage tensor as a measure of directional softening, definition of kinematics of the body, constitutive postulates and constitutive relations with a complete definition of material functions for an adiabatic process are included.

Section 4 comprises description of the numerical modelling. The material model implementation in a finite element software Abaqus by using the VUMAT user subroutine is discussed. The numerical calibration of the material model for DH-36 steel is presented. Finally, the definition of the numerical model for Nowacki's experimental set-up with numerical results of the specimen shearing are shown.

## 2. Nowacki's double shear test

Let us focus the attention on the variation of the Nowacki's double shear test for the high strain rates where loading results from the direct impact in Hopkinson transmitter tube (Klepaczko, 1994). The main advantage of the test considered is that for this type of loading path, large strains without the occurrence of a plastic instability are obtained and the application of the Hopkinson tube assures the reduction of Pochhammer-Chree vibrations what makes easier the constitutive modelling.

The crucial element of the whole experimental set-up is the special device which transforms the compression into nearly homogeneous shear over the total length of the specimen, see Fig. 1. The shear device, following the description by Klepaczko *et al.* (1999), consists of two coaxial parts, the external stiff housing and the internal cylindrical element. Both parts of this device are divided into two symmetrical clamps. Between the clamps, the sheet specimen is fixed by robust tightening of eight screws (six in the external part and two in the internal cylinder). The direct impact imposed on the cylindrical part induces the deformation of zones of the specimen between the internal and external clamps of the device producing the state of plane shear in their bounds.

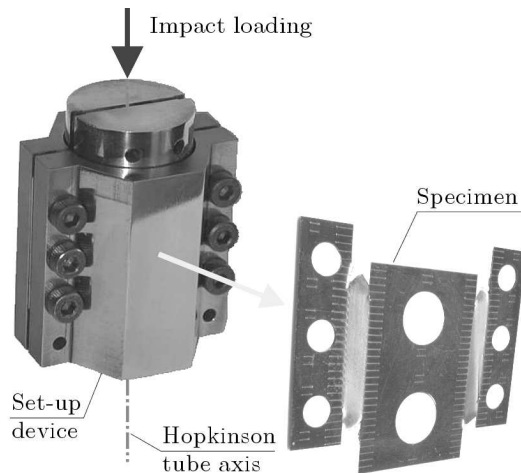


Fig. 1. Nowacki's double shear experimental set-up (Nowacki *et al.*, 2006)

This experimental technique (also called "block-bar" loading scheme in compression) enables investigation of the velocity of striker up to  $200 \text{ ms}^{-1}$ , giving global strain rates in the material tested reaching several thousands  $\text{s}^{-1}$ .

For the maximal velocities of the projectile, the intensity of plastic energy dissipation through the localised band can be so high, that the temperature generated exceeds the melting point leading to the phase change of the material tested – what states as a base for modern material modelling including except elastic and inelastic ranges also the phase change. Nevertheless, the device can also be used for quasi-static conditions, so one can be sure of the reliability of experimental results, with a substantial reduction of scatter.

During the experimental tests for advanced deformations, shear localisation zones are observed. Through the localised shear bands, the intensification of the intrinsic anisotropic microdamage process evolution is evidenced leading to final fracture (loss of continuity) in the specimen. Such results are fundamental for proper constitutive description of damage.

It should be emphasised that the method described imposes the following restrictions on geometry of the specimen (see Fig. 2):

- length of the double shear specimen allowed by the shear device is up to  $l_0 = 30$  mm,
- the shear zone should satisfy the condition:  $2 < a_0/t < 10$  to avoid buckling of the sheared zone and damage of the specimen during fixation in the device ( $t$  denotes the sheet thickness) and  $a_0/l_0 \leq 10^{-1}$  to minimise the error due to non-homogeneity of the shear stresses and strains at both ends of the specimen.

The common specimen dimensions, which are also assumed in Section 4 concerning numerical analysis, are presented in Fig. 2.

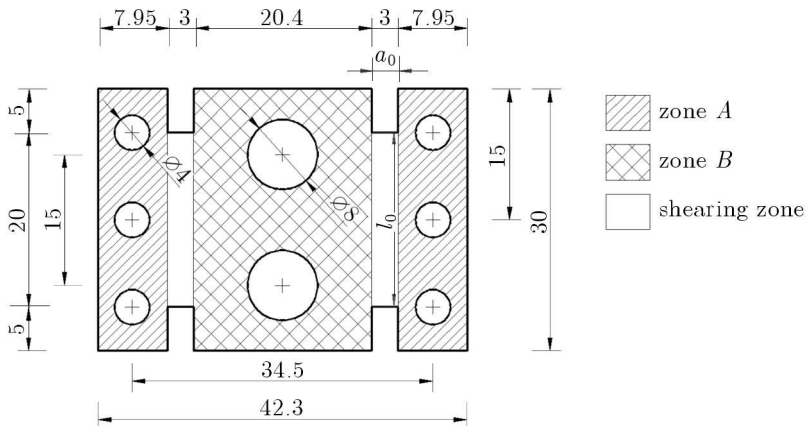


Fig. 2. Geometry of the specimen

### 3. Constitutive model

#### 3.1. Intrinsic anisotropic microdamage process

##### 3.1.1. Experimental motivation

Now, let us focus the attention on experimental observations of microdamage anisotropy in metals being the source of the overall metal anisotropy. Other sources of anisotropy like different sizes and shapes of adjacent grains (Narayanasamy *et al.*, 2009), presence of different phases like pearlite or ferrite (Pęcherski *et al.*, 2009) are not discussed.

So, the always existing defects in metal structures like microcracks, microvoids, mobile and immobile dislocations densities (Abu-Al-Rub and Voyiadjis, 2006; Voyiadjis and Abu-Al-Rub, 2006), see Fig. 3, cause anisotropy of metals. The anisotropy plays the fundamental role concerning damage phenomena. It is then clear, that for proper mathematical modelling of the metal behaviour one should include the anisotropy description. The frequently used isotropic simplification for metals should be thought of as a first approximation which carries not enough information for modern applications (Glema *et al.*, 2010); though it certainly does not disavow such an approach in many applications cf. Klepaczko (2007), Rusinek and Klepaczko (2009).

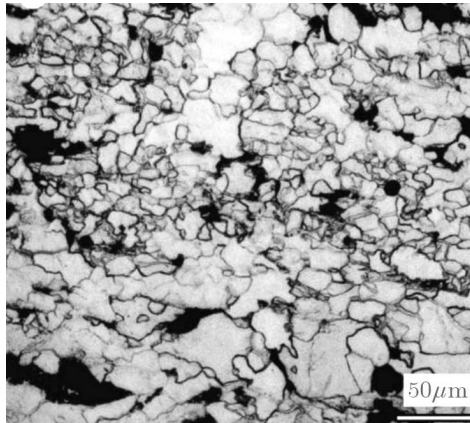


Fig. 3. Anisotropy of HSLA-65 steel microstructure (Narayanasamy *et al.*, 2009)

Coming back to the experimental results, being the crux of the matter of this section, showing the anisotropy of microdamages, we propose the following two statements (Sumelka, 2009):

- (i) intrinsic microdefects are anisotropic,
- (ii) evolution of microdamages is directional.

Statement (i) confirms the experimental results that the anisotropy in metals caused by the intrinsic defects, comes not only from their existence but especially from their inhomogeneous structure.

As an example, let us consider the effects of flat plate impact experiment in 1145 aluminium (Seaman, 1976). The separation observed is preceded by the evolution of microdamages (microvoids), consisting for the undamaged material of three stages: nucleation, growth and coalescence. Notice in Fig. that all of the microdefects are elongated perpendicularly to the impact direction, thus to the maximal tensile stresses. In this experiment, they have approximately an ellipsoidal shape. So, intrinsic defects have a directional nature. Their anisotropy influences the whole deformation process, having a considerable impact on it.

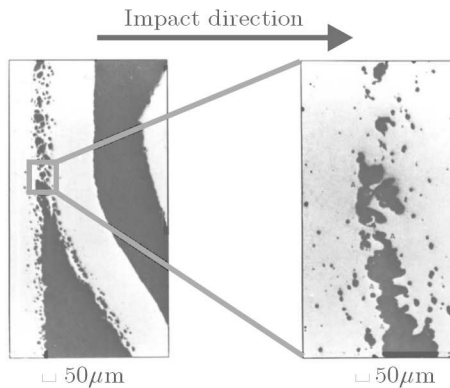


Fig. 4. Cracks anisotropy in 1145 aluminium after flat plate impact experiment (Seaman, 1976)

For the constitutive modelling purposes, we apply in the material model the directional measure for microdamage, since what causes the obtained model is more reliable. Notice that commonly used isotropic damage assumption (thought as ideally spherical microdamage assumption) is no longer valid for today's sophisticated industrial requirements. With such an approximation, we lose the information on the directions of microstructure evolution. In consequence, one can not predict damage directions or final failure modes with satisfactory accuracy.

Statement (ii) explicitly expresses the experimental fact that the anisotropic properties of a body of continuum evolve anisotropically during the deformation process (cf. experimental results presented by Grebe *et al.*, 1985). Notice, that it is a consequence of the structure rearrangement itself, but especially, by directional evolution of intrinsic defects. As an example in Fig. 5, the

evolution of microvoids in the region of forming of the shear band is presented. It is clearly seen that the evolution is directional, microvoids are being elongated through the shear band. So, the existing or nucleating growth of microdamages is directional according to the imposed deformation process, inducing the anisotropic evolution of material properties.

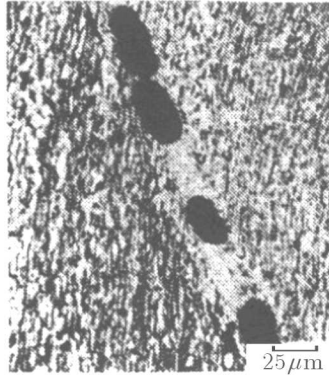


Fig. 5. Anisotropic microcracks in the shear band region in Ti-6 pct Al-4 pct V alloy (after Grebe *et al.*, 1985)

Thus, for purposes of constitutive modelling, the material model should take into consideration not only the anisotropy of microdamage but also its anisotropic evolution. Such an approach is the most natural and bases on the experimental results discussed.

As a concluding remark of this section, let us recall that the microdamage evolution mechanism in metals has generally three stages: defects nucleation, their growth and coalescence. All of them are anisotropic and should be described by the material model. The concept of microdamage tensor which fulfils all those requirements is presented in the next section.

### 3.1.2. Concept of microdamage tensor

As an introductory remark for constitutive modelling, notice that the material model presented is stated in terms of continuum mechanics in the framework of the thermodynamical theory of viscoplasticity together with the phenomenological approach by Perzyna (2008), Glema *et al.* (2009), Sumelka and Glema (2009). Formally, the constitutive structure belongs to the class of simple materials with fading memory, and due to its final form and the way of incorporating the fundamental variables, belongs to materials of the rate type with internal state variables (Truesdell and Noll, 1965). Such an approach

locates the model in macro (meso-macro) space scale, thus all variables in the model reflect the homogenised reaction from smaller scales of observations.

So, the modelling of microstructure in terms of continuum mechanics causes that we replace real micro geometry of its structure (its anisotropic nature) by directions of tensorial field. We introduce the *microdamage tensorial field* of the second order (as a state variable), denoting it by  $\xi$ , cf. Perzyna (2008), Glema *et al.* (2009), Sumelka (2009), which reflects the experimentally observed anisotropy of metals in the mathematical (constitutive) model.

The concept of microdamage tensor is constructed as follows.

Let us suppose that for selected points  $P_i$  in material body  $\mathcal{B}$ , on three perpendicular planes, the ratio of the damaged area to the assumed characteristic area of the representative volume element (RVE) can be measured, i.e.

$$\frac{A_i^p}{A} \tag{3.1}$$

where  $A_i^p$  is the damaged area and  $A$  denotes the assumed characteristic area of the RVE, see Fig. 6. Based on the calculated ratios  $(A_i^p/A)$ , three vectors are calculated. Their modules are equal to those ratios and are normal to RVE planes (see Fig. 6).

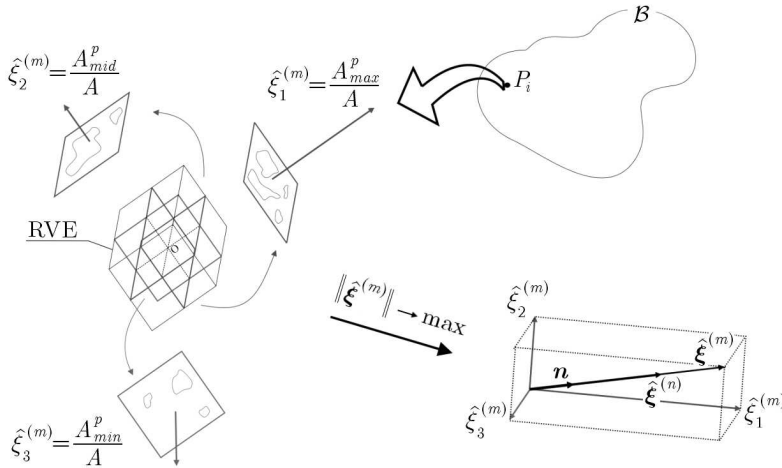


Fig. 6. The concept of microdamage tensor

Such measurements can be repeated in any different configuration obtained by the rotation of those three planes through point  $O$ , Fig. 6. So, for every measurement configuration, from those three vectors, we compose the resultant. Next, we choose such a configuration in which the resultant module

is the largest one. Such a resultant is called the *main microdamage vector* and is denoted by  $\widehat{\boldsymbol{\xi}}^{(m)}$  (Sumelka and Glema, 2007), i.e.

$$\widehat{\boldsymbol{\xi}}^{(m)} = \frac{A_1^p}{A} \widehat{\mathbf{e}}_1 + \frac{A_2^p}{A} \widehat{\mathbf{e}}_2 + \frac{A_3^p}{A} \widehat{\mathbf{e}}_3 \tag{3.2}$$

where  $\widehat{(\cdot)}$  denotes the principal directions of microdamage, and  $A_1^p \geq A_2^p \geq A_3^p$ .

In the following step, based on the main microdamage vector, we build a vector called the *microdamage vector*, denoted by  $\widehat{\boldsymbol{\xi}}^{(n)}$  (Sumelka and Glema, 2007)

$$\widehat{\boldsymbol{\xi}}^{(n)} = \frac{1}{\|\widehat{\boldsymbol{\xi}}^{(m)}\|} \left[ \left(\frac{A_1^p}{A}\right)^2 \widehat{\mathbf{e}}_1 + \left(\frac{A_2^p}{A}\right)^2 \widehat{\mathbf{e}}_2 + \left(\frac{A_3^p}{A}\right)^2 \widehat{\mathbf{e}}_3 \right] \tag{3.3}$$

Finally, we postulate the existence of microdamage tensorial field  $\boldsymbol{\xi}$

$$\boldsymbol{\xi} = \begin{bmatrix} \xi_{11} & \xi_{12} & \xi_{13} \\ \xi_{21} & \xi_{22} & \xi_{23} \\ \xi_{31} & \xi_{32} & \xi_{33} \end{bmatrix} \tag{3.4}$$

which we define in its principal directions by applying the formula combining the microdamage vector and microdamage tensor (Sumelka and Glema, 2007)

$$\widehat{\boldsymbol{\xi}}^{(n)} = \widehat{\boldsymbol{\xi}} \mathbf{n} \tag{3.5}$$

where

$$\mathbf{n} = \sqrt{3} \|\widehat{\boldsymbol{\xi}}^{(m)}\|^{-1} (\widehat{\xi}_1^{(m)} \widehat{\mathbf{e}}_1 + \widehat{\xi}_2^{(m)} \widehat{\mathbf{e}}_2 + \widehat{\xi}_3^{(m)} \widehat{\mathbf{e}}_3) \tag{3.6}$$

and the fundamental result that

$$\widehat{\boldsymbol{\xi}} = \frac{\sqrt{3}}{3} \begin{bmatrix} \widehat{\xi}_1^{(m)} & 0 & 0 \\ 0 & \widehat{\xi}_2^{(m)} & 0 \\ 0 & 0 & \widehat{\xi}_3^{(m)} \end{bmatrix} \tag{3.7}$$

So, we arrive at the following physical interpretation of the components of microdamage tensor: *The diagonal components  $\xi_{ii}$  of microdamage tensor  $\boldsymbol{\xi}$  in its principal directions are proportional to the components of the main microdamage vector  $\widehat{\xi}_i^{(m)}$ , which defines the ratio of the damaged area to the assumed characteristic area of the RVE on the plane perpendicular to the direction  $i$ .*

Moreover, taking the Euclidean norm from the microdamage field  $\widehat{\boldsymbol{\xi}}$ , we obtain

$$\sqrt{\boldsymbol{\xi} : \boldsymbol{\xi}} = \frac{\sqrt{3}}{3} \sqrt{\left(\frac{A_1^p}{A}\right)^2 + \left(\frac{A_2^p}{A}\right)^2 + \left(\frac{A_3^p}{A}\right)^2} \tag{3.8}$$

Now, assuming that the characteristic length of RVE cube is  $l$  we can rewrite Eq. (3.8) as

$$\sqrt{\boldsymbol{\xi} : \boldsymbol{\xi}} = \frac{\frac{\sqrt{3}l^2}{3} \sqrt{(A_1^p)^2 + (A_2^p)^2 + (A_3^p)^2}}{l^3} \quad (3.9)$$

From Eq. (3.8), another physical interpretation for microdamage tensor appears. Namely, the Euclidean norm of the microdamage field defines the scalar quantity called the *volume fraction porosity* or simply *porosity* (Perzyna 2006, 2008)

$$\sqrt{\boldsymbol{\xi} : \boldsymbol{\xi}} = \xi = \frac{V - V_s}{V} = \frac{V_p}{V} \quad (3.10)$$

where  $\xi$  denotes porosity (scalar damage parameter),  $V$  is the volume of a material element and  $V_s$  is the volume of the solid constituent of that material element and  $V_p$  denotes the void volume

$$V_p = \frac{\sqrt{3}}{3} l^2 \sqrt{(A_1^p)^2 + (A_2^p)^2 + (A_3^p)^2} \quad (3.11)$$

Notice that the interpretations of the microdamage tensorial field impose mathematical bounds for microdamage evolution, namely

$$\xi \in \langle 0, 1 \rangle \quad \text{and} \quad \hat{\xi}_{ii} \in \langle 0, 1 \rangle \quad (3.12)$$

However the physical bounds are different. The experimental evidence shows that there exists the initial porosity (denoted by  $\xi_0$ ) which in metals is of order  $\xi_0 \cong 10^{-4}$ - $10^{-3}$  (Nemes and Eftis, 1991) and also, that the porosity can not reach the theoretical full saturation, i.e.  $\xi = 1$ , during the deformation process. The real maximal fracture porosity depends then on the material tested and is of order 0.09-0.35 (Dorn and Perzyna, 2002a,b, 2006).

### 3.2. Constitutive model for an adiabatic process

The key features of the formulation presented are: (i) the description is invariant with respect to any diffeomorphism (the obtained model in covariant (Marsden and Hughes, 1983), (ii) well-posedness of the obtained regularization evolution problem, (iii) rate sensitivity, (iv) finite elasto-viscoplastic deformations, (v) plastic non-normality, (vi) dissipation effects, (vii) thermo-mechanical couplings and (viii) length scale sensitivity. Below, the fundamental results for an adiabatic process are given – for detailed and more general formulation see Sumelka (2009).

The abstract body is a differential manifold. The kinematics of the body assumes finite elasto-viscoplastic deformations which are governed by multiplicative decomposition of the total deformation gradient to elastic and viscoplastic parts (Lee, 1969; Perzyna, 1995)

$$\mathbf{F}(\mathbf{X}, t) = \mathbf{F}^e(\mathbf{X}, t)\mathbf{F}^p(\mathbf{X}, t) \quad (3.13)$$

In (3.13)  $\mathbf{F} = \partial\phi(\mathbf{X}, t)/\partial\mathbf{X}$  is the deformation gradient,  $\phi$  describes motion,  $\mathbf{X}$  denotes material coordinates,  $t$  is time and  $\mathbf{F}^e$ ,  $\mathbf{F}^p$  are elastic and viscoplastic parts, respectively.

From the spatial deformation gradient, denoted by  $\mathbf{l}$

$$\mathbf{l}(\mathbf{x}, t) = \frac{\partial\mathbf{v}(\mathbf{x}, t)}{\partial\mathbf{x}} \quad (3.14)$$

where  $\mathbf{v}$  denotes the spatial velocity and  $\mathbf{x}$  are spatial coordinates, taking its decomposition to symmetric and antisymmetric parts, we obtain

$$\begin{aligned} \mathbf{l} &= \mathbf{d} + \mathbf{w} = \mathbf{d}^e + \mathbf{w}^e + \mathbf{d}^p + \mathbf{w}^p \\ \mathbf{d} &= \frac{1}{2}(\mathbf{l} + \mathbf{l}^\top) \quad \mathbf{w} = \frac{1}{2}(\mathbf{l} - \mathbf{l}^\top) \end{aligned} \quad (3.15)$$

Now taking the Lie derivative of the assumed strain measure (the Euler-Almansi strain), we have the relation

$$\mathbf{d}^b = L_v(\mathbf{e}^b) \quad (3.16)$$

and simultaneously

$$\mathbf{d}^{e^b} = L_v(\mathbf{e}^{e^b}) \quad \mathbf{d}^{p^b} = L_v(\mathbf{e}^{p^b}) \quad (3.17)$$

where  $L_v$  stands for the Lie derivative and  $\mathbf{e}$  for the Euler-Almansi strain, showing the fundamental result that the symmetric part of spatial deformation gradient is directly the Lie derivative of the Euler-Almansi strain. Notice that the following constitutive structure operates in spatial configuration. The spatial covariance of the model mentioned is just due to consequently making use of the Lie derivative.

Next, assuming that the balance principles hold, namely: conservation of mass, balance of momentum, balance of moment of momentum and balance of energy, and the entropy production inequality is satisfied, we define four constitutive postulates (Perzyna, 2005):

- (i) The existence of the free energy function  $\psi$ . Formally, we apply the following form

$$\psi = \widehat{\psi}(\mathbf{e}, \mathbf{F}, \vartheta; \boldsymbol{\mu}) \quad (3.18)$$

where  $\boldsymbol{\mu}$  denotes a set of internal state variables that govern the description of dissipation effects, and  $\vartheta$  is temperature.

- (ii) The axiom of objectivity (spatial covariance). The material model should be invariant with respect to any superposed motion (diffeomorphism).
- (iii) The axiom of the entropy production. For every regular process, the constitutive functions should satisfy the second law of thermodynamics.
- (iv) The evolution equation for the internal state variable vector  $\boldsymbol{\mu}$  should be of the form

$$L_{\mathbf{v}}\boldsymbol{\mu} = \widehat{m}(\mathbf{e}, \mathbf{F}, \vartheta, \boldsymbol{\mu}) \quad (3.19)$$

where evolution function  $\widehat{m}$  has to be determined based on the experimental observations.

The determination of  $\widehat{m}$  appears the most challenge problem in modern constitutive modelling.

The explicit statement of the complete set of governing equations for an adiabatic process we precede by additional assumptions, see Dorn and Perzyna (2002a,b), Perzyna (2005), Glema *et al.* (2008), Sumelka and Glema (2009), Sumelka (2009):

- (i) microdamage does not considerably influence the elastic range,
- (ii) in every material point of the body there exists the initial microdamage state,
- (iii) conductivity and thermo-elastic effects are omitted.

Assuming that the above holds, the body under going deformation in an adiabatic regime is governed by the following set of equations. They state the initial boundary value problem (IBVP).

Find  $\phi$ ,  $\mathbf{v}$ ,  $\rho$ ,  $\boldsymbol{\tau}$ ,  $\boldsymbol{\xi}$ ,  $\vartheta$  as functions of  $t$  and position  $\mathbf{x}$  such that (Perzyna, 1994; Łodygowski, 1996; Łodygowski and Perzyna, 1997a,b):

(i) the field equations

$$\begin{aligned}
 \dot{\phi} &= \mathbf{v} \\
 \dot{\mathbf{v}} &= \frac{1}{\rho_{Ref}} \left[ \operatorname{div} \boldsymbol{\tau} + \frac{\boldsymbol{\tau}}{\rho} \cdot \operatorname{grad} \rho - \frac{\boldsymbol{\tau}}{1 - (\boldsymbol{\xi} : \boldsymbol{\xi})^{\frac{1}{2}}} \operatorname{grad} (\boldsymbol{\xi} : \boldsymbol{\xi})^{\frac{1}{2}} \right] \\
 \dot{\rho} &= -\rho \operatorname{div} \mathbf{v} + \frac{\rho}{1 - (\boldsymbol{\xi} : \boldsymbol{\xi})^{\frac{1}{2}}} (L_v \boldsymbol{\xi} : L_v \boldsymbol{\xi})^{\frac{1}{2}} \\
 \dot{\boldsymbol{\tau}} &= \mathcal{L}^e : \mathbf{d} + 2\boldsymbol{\tau} \cdot \mathbf{d} - \mathcal{L}^{th} \dot{\vartheta} - (\mathcal{L}^e + \mathbf{g}\boldsymbol{\tau} + \boldsymbol{\tau}\mathbf{g}) : \mathbf{d}^p \\
 \dot{\boldsymbol{\xi}} &= 2\boldsymbol{\xi} \cdot \mathbf{d} + \frac{\partial g^*}{\partial \boldsymbol{\tau}} \frac{1}{T_m} \left\langle \Phi^g \left[ \frac{I_g}{\tau_{eq}(\boldsymbol{\xi}, \vartheta, \epsilon^p)} - 1 \right] \right\rangle \\
 \dot{\vartheta} &= \frac{\chi^*}{\rho c_p} \boldsymbol{\tau} : \mathbf{d}^p + \frac{\chi^{**}}{\rho c_p} \mathbf{k} : L_v \boldsymbol{\xi}
 \end{aligned} \tag{3.20}$$

(ii) the boundary conditions

- (a) displacement  $\phi$  is prescribed on the part  $\Gamma_\phi$  of  $\Gamma(\mathcal{B})$  and tractions  $(\boldsymbol{\tau} \cdot \mathbf{n})^a$  are prescribed on the part  $\Gamma_\tau$  of  $\Gamma(\mathcal{B})$ , where  $\Gamma_\phi \cap \Gamma_\tau = \emptyset$  and  $\Gamma_\phi \cup \Gamma_\tau = \Gamma(\mathcal{B})$
- (b) heat flux  $\mathbf{q} \cdot \mathbf{n} = 0$  is prescribed on  $\Gamma(\mathcal{B})$

(iii) the initial conditions  $\phi, \mathbf{v}, \rho, \boldsymbol{\tau}, \boldsymbol{\xi}, \vartheta$  are given for each particle  $\mathbf{X} \in \mathcal{B}$  at  $t = 0$ ,

are satisfied. In the above we denoted:  $\rho_{Ref}$  a referential density,  $\boldsymbol{\tau}$  – Kirchhoff stress tensor,  $\rho$  – current density,  $\mathcal{L}^e$  – elastic constitutive tensor,  $\mathcal{L}^{th}$  – thermal operator,  $\mathbf{g}$  – metric tensor,  $\partial g^* / \partial \boldsymbol{\tau}$  – evolution directions for anisotropic microdamage growth processes,  $T_m$  – relaxation time,  $I_g$  – stress intensity invariant,  $\tau_{eq}$  – threshold stress,  $\chi^*, \chi^{**}$  – irreversibility coefficients and  $c_p$  – specific heat.

For evolution problem (3.20), we assume as follows:

1. For the elastic constitutive tensor  $\mathcal{L}^e$

$$\mathcal{L}^e = 2\mu \mathcal{I} + \lambda(\mathbf{g} \otimes \mathbf{g}) \tag{3.21}$$

where  $\mu, \lambda$  are Lamé constants.

2. For the thermal operator  $\mathcal{L}^{th}$

$$\mathcal{L}^{th} = (2\mu + 3\lambda)\theta \mathbf{g} \tag{3.22}$$

where  $\theta$  is the thermal expansion coefficient.

3. For the viscoplastic flow phenomenon  $\mathbf{d}^p$  (Perzyna, 1963, 1966)

$$\mathbf{d}^p = \Lambda^{vp} \mathbf{p} \tag{3.23}$$

where

$$\begin{aligned} \Lambda^{vp} &= \frac{1}{T_m} \left\langle \Phi^{vp} \left( \frac{f}{\kappa} - 1 \right) \right\rangle = \frac{1}{T_m} \left\langle \left( \frac{f}{\kappa} - 1 \right)^{m_{pl}} \right\rangle \\ f &= \left\{ J_2' + [n_1(\vartheta) + n_2(\vartheta)(\boldsymbol{\xi} : \boldsymbol{\xi})^{\frac{1}{2}}] J_1^2 \right\}^{\frac{1}{2}} \\ n_1(\vartheta) &= 0 \qquad n_2(\vartheta) = n = \text{const} \\ \kappa &= \{ \kappa_s(\vartheta) - [\kappa_s(\vartheta) - \kappa_0(\vartheta)] \exp[-\delta(\vartheta)\epsilon^p] \} \left[ 1 - \left( \frac{(\boldsymbol{\xi} : \boldsymbol{\xi})^{\frac{1}{2}}}{\xi_F} \right)^{\beta(\vartheta)} \right] \tag{3.24} \\ \bar{\vartheta} &= \frac{\vartheta - \vartheta_0}{\vartheta_0} \qquad \kappa_s(\vartheta) = \kappa_s^* - \kappa_s^{**} \bar{\vartheta} \qquad \kappa_0(\vartheta) = \kappa_0^* - \kappa_0^{**} \bar{\vartheta} \\ \delta(\vartheta) &= \delta^* - \delta^{**} \bar{\vartheta} \qquad \beta(\vartheta) = \beta^* - \beta^{**} \bar{\vartheta} \\ \mathbf{p} &= \frac{\partial f}{\partial \boldsymbol{\tau}} \Big|_{\boldsymbol{\xi} = \text{const}} \left( \left\| \frac{\partial f}{\partial \boldsymbol{\tau}} \right\| \right)^{-1} = \frac{1}{[2J_2' + 3A^2(\text{tr } \boldsymbol{\tau})^2]^{\frac{1}{2}}} [\boldsymbol{\tau}' + A \text{tr } \boldsymbol{\tau} \boldsymbol{\delta}] \\ \xi^F &= \xi^{F*} - \xi^{F**} \left\langle \left( \frac{\|L_v \boldsymbol{\xi}\| - \|L_v \boldsymbol{\xi}_c\|}{\|L_v \boldsymbol{\xi}_c\|} \right)^{m_F} \right\rangle \end{aligned}$$

and  $f$  denotes potential function (Shima and Oyane, 1976; Perzyna, 1986a,b; Glema *et al.*, 2009),  $\kappa$  is isotropic workhardeningsoftening function (Perzyna, 1986b; Nemes and Eftis, 1993; Glema *et al.*, 2006),  $\boldsymbol{\tau}'$  – stress deviator,  $J_1, J_2'$  are the first and second invariants of the Kirchhoff stress tensor and the deviatoric part of the Kirchhoff stress tensor, respectively,  $A = 2(n_1 + n_2(\boldsymbol{\xi} : \boldsymbol{\xi})^{\frac{1}{2}})$ ,  $\xi^{F*}$  can be thought as quasi-static fracture porosity and  $\|L_v \boldsymbol{\xi}_c\|$  denotes the equivalent critical velocity of microdamage. Notice that Eqs. (3.24)<sub>12</sub> reflects an experimental fact that the fracture porosity changes for fast processes. Such an approach is consistent with the so called cumulative fracture criterion (Campbell, 1953, Klepaczko, 1990), namely there exists a critical time needed for saturation of microdamage to its fracture limit.

4. For the microdamage mechanism, assume the additional conditions (Dornowski, 1999; Glema *et al.*, 2006, 2009):

- an increment in the microdamage state is coaxial with the principal directions of the stress state,
- only the positive principal stresses induce growth of the microdamage,

thus we have

$$\frac{\partial g^*}{\partial \boldsymbol{\tau}} = \left\langle \frac{\partial \hat{g}}{\partial \boldsymbol{\tau}} \right\rangle \left\| \left\langle \frac{\partial \hat{g}}{\partial \boldsymbol{\tau}} \right\rangle \right\|^{-1} \quad \hat{g} = \frac{1}{2} \boldsymbol{\tau} : \boldsymbol{\mathcal{G}} : \boldsymbol{\tau} \quad (3.25)$$

$$\Phi^g \left( \frac{I_g}{\tau_{eq}(\boldsymbol{\xi}, \vartheta, \epsilon^p)} - 1 \right) = \left( \frac{I_g}{\tau_{eq}} - 1 \right)^{m_{md}}$$

where

$$\tau_{eq} = c(\vartheta) [1 - (\boldsymbol{\xi} : \boldsymbol{\xi})^{\frac{1}{2}}] \ln \frac{1}{(\boldsymbol{\xi} : \boldsymbol{\xi})^{\frac{1}{2}}} \{ 2\kappa_s(\vartheta) - [\kappa_s(\vartheta) - \kappa_0(\vartheta)] F(\xi_0, \boldsymbol{\xi}, \vartheta) \}$$

$$c(\vartheta) = \text{const} \quad (3.26)$$

$$F = \left( \frac{\xi_0}{1 - \xi_0} \frac{1 - (\boldsymbol{\xi} : \boldsymbol{\xi})^{\frac{1}{2}}}{(\boldsymbol{\xi} : \boldsymbol{\xi})^{\frac{1}{2}}} \right)^{\frac{2}{3}\delta} + \left( \frac{1 - (\boldsymbol{\xi} : \boldsymbol{\xi})^{\frac{1}{2}}}{1 - \xi_0} \right)^{\frac{2}{3}\delta}$$

and

$$I_g = \bar{b}_1 J_1 + \bar{b}_2 (J_2)^{\frac{1}{2}} + \bar{b}_3 (J_3)^{\frac{1}{3}} \quad (3.27)$$

$\bar{b}_i$  ( $i = 1, 2, 3$ ) are material parameters,  $J_3$  is the third invariant of deviatoric part of the Kirchhoff stress tensor.

Now, taking into account the postulates for microdamage evolution, and assuming that the tensor  $\boldsymbol{\mathcal{G}}$  can be written as a symmetric part of the fourth order unity tensor  $\boldsymbol{\mathcal{I}}$  (Łodygowski *et al.*, 2008), i.e.

$$\boldsymbol{\mathcal{G}} = \boldsymbol{\mathcal{I}}^s \quad \mathcal{G}_{ijkl} = \frac{1}{2} (\delta_{ik} \delta_{jl} + \delta_{il} \delta_{jk}) \quad (3.28)$$

we can write the explicit form of the growth function  $\hat{g}$  as

$$\hat{g} = \frac{1}{2} (\tau_I^2 + \tau_{II}^2 + \tau_{III}^2) \quad (3.29)$$

The gradient of  $\hat{g}$  with respect to the stress field gives us the following matrix representation of the tensor describing the anisotropic evolution of microdamage

$$\frac{\partial \hat{g}}{\partial \boldsymbol{\tau}} = \begin{bmatrix} g_{11} \tau_I & 0 & 0 \\ 0 & g_{22} \tau_{II} & 0 \\ 0 & 0 & g_{33} \tau_{III} \end{bmatrix} \quad (3.30)$$

In (3.30),  $\tau_I, \tau_{II}, \tau_{III}$  are the principal values of the Kirchhoff stress tensor.

Notice that the definition of the threshold stress for the microcrack growth function  $\tau_{eq}$  indicates that the growth term in the evolution function for microdamage is active only after nucleation – before nucleation we have an infinite threshold  $\lim_{\boldsymbol{\xi} \rightarrow \mathbf{0}} \tau_{eq} = \infty$ .

5. For temperature evolution, Eqs. (3.20), we take

$$\mathbf{k} = \boldsymbol{\tau} \quad (3.31)$$

To conclude this Section, notice that evolution problem (3.20) is well-posed (Łodygowski *et al.*, 1994; Łodygowski, 1995, 1996). The relaxation time  $T_m$  can be viewed as a regularization parameter which implicitly introduces the length scale. Thus, it can be proved (Łodygowski, 1996; Glema, 2004) that the so called Cauchy problem, defined above, has a unique and stable solution.

## 4. Numerical analysis

### 4.1. Material model implementation

The solution to the IBVP defined by Eqs. (3.20) has been obtained by using the finite element method. Abaqus/Explicit commercial finite element code has been adapted as a solver. The model has been implemented in the software by taking advantage of user subroutine VUMAT, which is coupled with Abaqus system [1]. Abaqus/Explicit uses the central-difference time integration rule together with diagonal ("lumped") element mass matrices.

Some comments are needed on the stress update in VUMAT user subroutine. During computations, user subroutine VUMAT controls the evolution of stresses, viscoplastic deformation, temperature and microdamage fields. Recall that in the presented material model, the Lie derivative has been taken into account for all rates, including the stress rate. Hence

$$L_v \boldsymbol{\tau} = \dot{\boldsymbol{\tau}} - \mathbf{I}^\top \boldsymbol{\tau} - \boldsymbol{\tau} \mathbf{I} \quad (4.1)$$

while in contrast, in Abaqus/Explicit VUMAT user subroutine, the Green-Naghdi rate is calculated by default, through the following formula [1]

$$\boldsymbol{\tau}^{(G-N)^\circ} = \dot{\boldsymbol{\tau}} + \boldsymbol{\tau} \boldsymbol{\Omega} - \boldsymbol{\Omega} \boldsymbol{\tau} \quad (4.2)$$

where  $\boldsymbol{\Omega} = \boldsymbol{\Omega}^{(G-N)} = \dot{\mathbf{R}} \mathbf{R}^\top$  represents the angular velocity of the material (Dienes, 1979) (or spin tensor (Xiao *et al.*, 1997)) and  $\mathbf{R}$  denotes the rotation tensor. The important is also that the material model in Abaqus/Explicit VUMAT user subroutine is defined in a corotational coordinate system, being described by the spin tensor  $\boldsymbol{\Omega}$  (see Fig. 7).

To keep the algorithm objective in the Lie sense in VUMAT user subroutine, we have applied the following approach. In the iterative procedure, we take

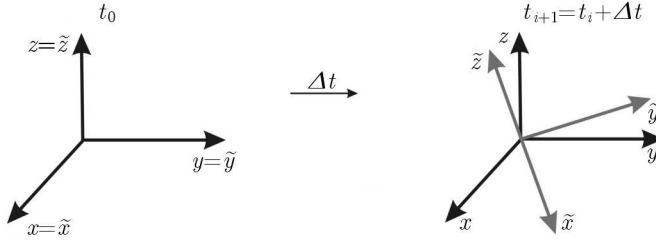


Fig. 7. Initial  $(XYZ)$  and corotational  $(\tilde{X}\tilde{Y}\tilde{Z})$  coordinate systems

for the material derivative of the second order tensor, the forward difference scheme. Thus, for the material derivative of the Kirchhoff stress tensor, we have

$$\dot{\tau}|_i = \frac{\tau|_{i+1} - \tau|_i}{\Delta t} \tag{4.3}$$

Using Eqs. (4.1) and (4.2), we can write in the corotational coordinate system, respectively

$$\tilde{\tau}|_{i+1} = \mathbf{R}^\top|_{i+1} [\tau|_i + \Delta t L_v \tau|_i + \Delta t (\mathbf{I}^\top|_i \tau|_i + \tau|_i \mathbf{I}|_i)] \mathbf{R}|_{i+1} \tag{4.4}$$

and

$$\tilde{\tau}|_{i+1} = \mathbf{R}^\top|_{i+1} [\tau|_i + \Delta t \tau^{(G-N)\circ}|_i + \Delta t (\boldsymbol{\Omega}|_i \tau|_i - \tau|_i \boldsymbol{\Omega}|_i)] \mathbf{R}|_{i+1} \tag{4.5}$$

Thus we see that the Green-Naghdi rate produces an additional term

$$\Delta t (\boldsymbol{\Omega}|_i \tau|_i - \tau|_i \boldsymbol{\Omega}|_i) \tag{4.6}$$

That is why one has to subtract this term if another rate is proposed. Hence, in the presented formulation for stress update in VUMAT, we have (Sumelka and Glema, 2009)

$$\tilde{\tau}|_{i+1} = \mathbf{R}^\top|_{i+1} [\tau|_i + \Delta t (2\tau|_i \mathbf{d}|_i + L_v \tau|_i) + \boldsymbol{\Upsilon}|_i] \mathbf{R}|_{i+1} \tag{4.7}$$

where  $\boldsymbol{\Upsilon}|_i = -\Delta t (\boldsymbol{\Omega}|_i \tau|_i - \tau|_i \boldsymbol{\Omega}|_i)$  and  $\tau|_i = \mathbf{R}|_i \tilde{\tau}|_i \mathbf{R}^\top|_i$ .

Such an approach is needed for stresses only because other variables are kept as scalars in VUMAT user subroutine. The detailed algorithm for the whole process can be found in Sumelka (2009).

#### 4.2. Numerical identification

To solve IBVP defined by Eqs. (3.20), one has to determine 28 unknown parameters, that characterise the analysed material (steel). In Table 1, we

present a complete set of parameters (identified in the sense of numerical calibration) for DH-36 steel. The identification procedure bases on the results obtained experimentally by Nemat-Nasser and Guo (2003). These parameters are used in the following section concerning numerical simulation of Nowacki's double shear test.

**Table 1.** Material parameters for DH-36 steel

$\lambda = 121.154 \text{ GPa}$	$\mu = 80.769 \text{ GPa}$	$\rho_{Ref} = 7800 \text{ kg/m}^3$	$m_{md} = 1$
$c = 0.067$	$b_1 = 0$	$b_2 = 0.5$	$b_3 = 0$
$\xi^{F*} = 0.36$	$\xi^{F**} = 0$	$m_{F-}$	$\ L_v \xi_c\  - s^{-1}$
$\delta^* = 6.0$	$\delta^{**} = 1.4$	$T_m = 2.5 \mu\text{s}$	$m_{pl} = 0.14$
$\kappa_s^* = 605 \text{ MPa}$	$\kappa_s^{**} = 137 \text{ MPa}$	$\kappa_0^* = 395 \text{ MPa}$	$\kappa_0^{**} = 90 \text{ MPa}$
$\beta^* = 11.0$	$\beta^{**} = 2.5$	$n_1 = 0$	$n_2 = 0.25$
$\chi^* = 0.8$	$\chi^{**} = 0.1$	$\theta = 10^{-6} \text{ K}^{-1}$	$c_p = 470 \text{ J/kgK}$

DH-36 steel belongs to the class of high strength structural low-alloy steels. This steel is commonly used in shipbuilding, thus it may be subjected to high-rate loading due to collision, impact or explosion connected with a wide range of temperatures. It is then natural that DH-36 steel distinguishes itself due to good weldability, toughness, good ductility and plasticity (true strain  $> 60\%$ ) under various temperatures and loading rates (see Nemat-Nasser and Guo, 2003), where a comprehensive experimental study of DH-36 over strain rates ranging from  $0.001 \text{ s}^{-1}$  to about  $800 \text{ s}^{-1}$  and simultaneously with initial temperatures ranging from  $77 \text{ K}$  to  $1000 \text{ K}$  is presented). The steel has characteristics of the bcc structure, hence it belongs to the so called ferritic steels. Mechanical properties of DH-36 steel are strongly affected by impurities in its internal structure. It is important that the processing (rolling) of DH-36 steel can induce anisotropy of its structure.

Figure 8 shows the adjustment of model predictions to experimental data. Notice that the numerical solution is obtained from full 3D thermomechanical analysis accounting for the anisotropic intrinsic microdamage process mentioned – in other words, the presented numerical results take into account the whole local process. The curve fitting shows that using the presented material model one can obtain numerical simulations in a very good agreement with experimental observations.

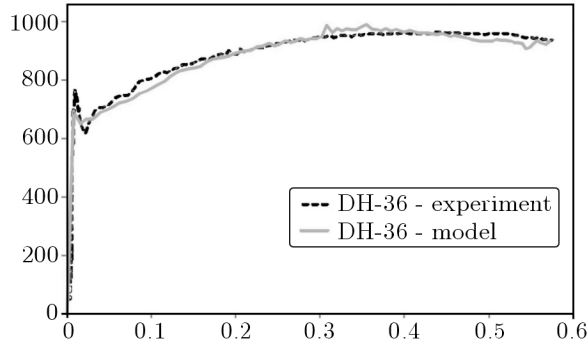


Fig. 8. Comparison of experimental (Nemat-Nasser and Guo, 2003) and numerical results for strain rate  $3000\text{s}^{-1}$  and initial temperature  $296\text{K}$

### 4.3. Numerical simulation of Nowacki's double shear test

#### 4.3.1. Computational model

The full spatial model of the specimen is under consideration. Geometry of the specimen is presented in Fig. 2. The thickness of the specimen is equal to  $0.64\text{mm}$ .

In zone *A* (cf. Fig. 2) at the bottom and upper planes of the specimen, the fixed boundary conditions were imposed. They model the part of Nowacki's device that is fixed (cf. Fig. 1). In zone *B* (cf. Fig. 2) we induced rigid motion of the bottom and upper planes of the specimen (using so called rigid body constraints in Abaqus) and, simultaneously, we added additional concentrated mass (equal  $0.5\text{kg}$ , see Klepaczko *et al.* (1999)) at the centre of gravity of the zone *B* which models the mass of movable part of Nowacki's device and the striker. Notice that this additional mass plays a meaningful role in proper modelling of the experiment.

To the rigid surfaces in zone *B*, an initial velocity of  $19.7\text{ms}^{-1}$  (Nowak *et al.*, 2007) and the initial temperature of  $296\text{K}$  was applied. Because of lack of the experimental data concerning the initial microdamage distribution in the specimen we assumed it to be equal in every material point in the body and, simultaneously, we assumed its initial isotropy. This simplification is crucial concerning the fact that the way of mapping of the initial microdamage state has a strong impact on the final failure mode and the global answer from the specimen (Sumelka, 2009). The components of microdamage tensor were chosen in a way to obtain the initial porosity equal to  $6 \cdot 10^{-4}$ , namely

$$\xi_0 = \begin{bmatrix} 34.64 \cdot 10^{-5} & 0 & 0 \\ 0 & 34.64 \cdot 10^{-5} & 0 \\ 0 & 0 & 34.64 \cdot 10^{-5} \end{bmatrix}$$

The contact plays an important part in the of modelling. It is due to strong concentrations at the corners of shear zones (the one at the pathway from the shear zone and the movable part of Nowacki's device, and at the pathway from the shear zone and the fixed part of Nowacki's device). At those corners, self contact occurs and has an influence in the direction of failure path. That is why the general contact in Abaqus/Explicit was applied, which assures the self contact conditions. The properties of contact were: hard normal contact (without penetration and unlimited contact stresses) and tangential contact with Coulomb's friction model (friction coefficient equal to 0.05).

The C3D8R finite elements (8-node linear brick, reduced integration element) were chosen for spatial discretisation with total 1.4 M dof for the specimen model.

#### 4.3.2. Results

Let us discuss and interpret the obtained results of the Huber-Mises-Hencky (HMH) stress, the shear stress, temperature, porosity and directions of microdamage fields in the selected time instance of a process. The time up to full damage is around 180  $\mu$ s.

In Figs. 9 and 10, HMH and shear stresses are presented (due to the symmetry, only a half of the model is shown in the following figures). One should notice that both mentioned fields indicate a homogeneous response during the test as long as the failure (loss of continuity) occurs from the corners. The important is that neither HMH stresses nor shear stresses can not be used as a failure predictor. Due to the homogeneous response in the shear zone, before discontinuity occurs, one can not estimate the failure pattern. Nevertheless, the fundamental result coming from the discussed stress fields are that the level of HMH stresses confirms the flow stresses observed in the experiment (cf. Fig. 8), while the shear stress level confirms the results from Nowacki's test that the resultant macro force acting on the specimen is around 900-1200 N (Nowacki *et al.*, 2006; Nowak *et al.*, 2007).

The temperature field versus time is presented in Fig. 11. It is clearly seen that due to viscoplastic deformation in the shear zone a substantial temperature rise is observed. In the strain localisation zones, the temperature reaches

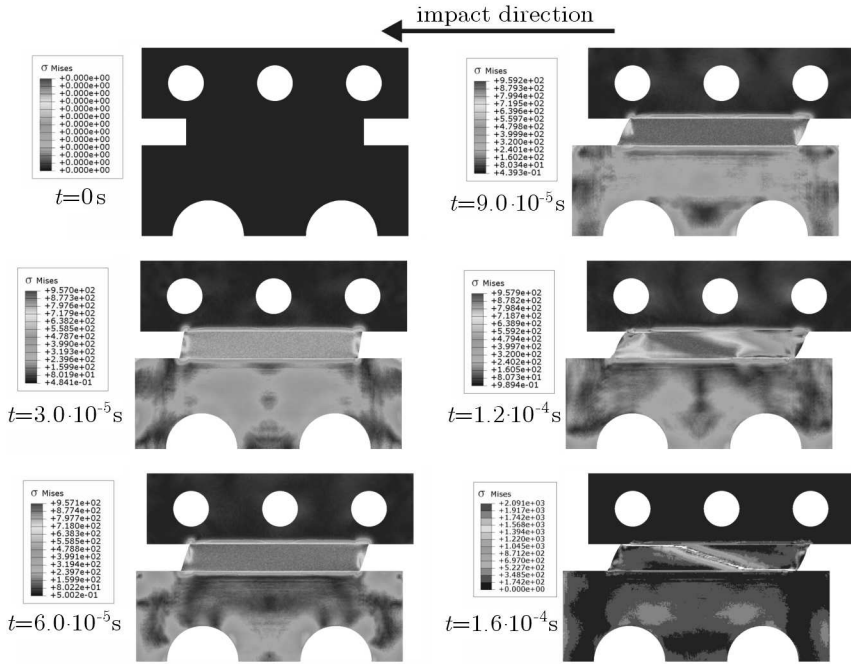


Fig. 9. HMH stresses evolution in Nowacki's specimen vs. time

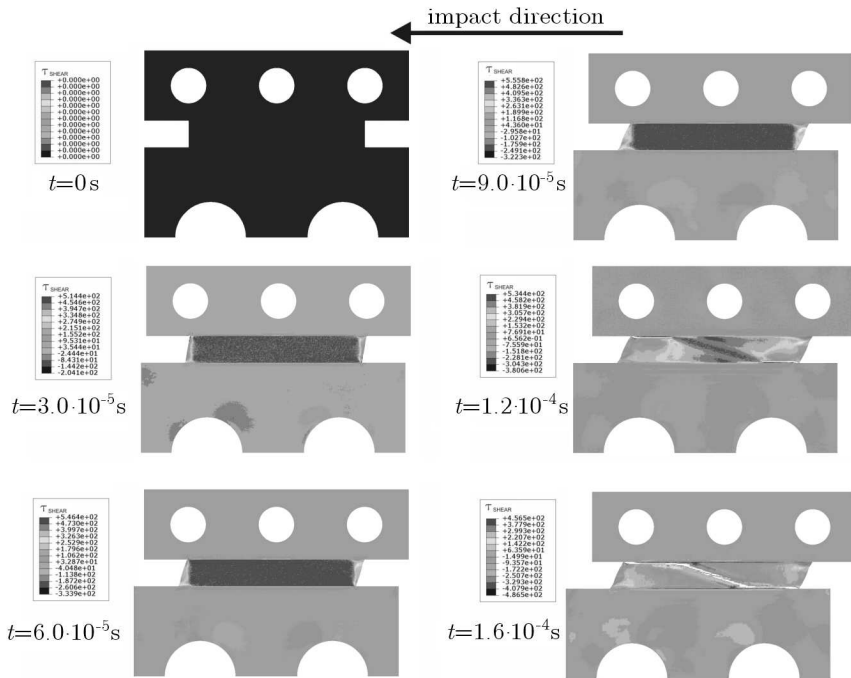


Fig. 10. Shear stresses evolution in Nowacki's specimen vs. time

around 900 K. It should be noticed that for the highest velocities of the striker the temperature rise can be so large that the melting point is reached in shear bands causing that no deformation is observed in the shear zone while the movable part of Nowacki's device moves through melted steel. This creates an interesting research area for consecutive modelling of metals including effects of phase transformation. Notice that the temperature field gives a better estimation for possible failure patterns (cf. Fig. 11).

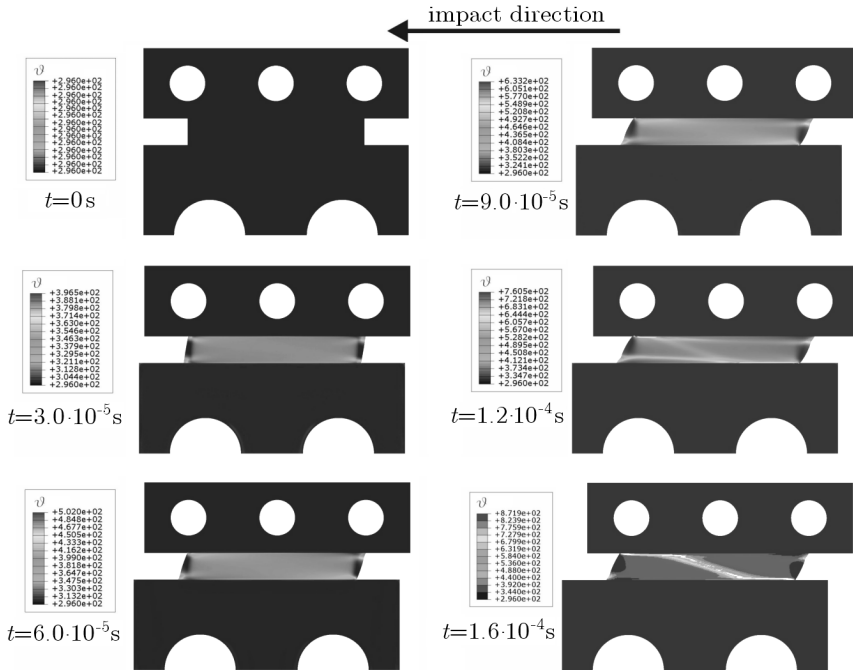


Fig. 11. Temperature evolution in Nowacki's specimen vs. time

In Fig. 12, the time history of porosity (being the norm of the intrinsic anisotropic microdamage measure) is presented. Similarly, as for the temperature field, this field gives a better estimation of the failure pattern in comparison to the stress one. Intensified zones of microdamage evolution in the corners of the specimen are seen. The fracture that occurs between  $90 \mu\text{s}$  and  $120 \mu\text{s}$  starts its evolution exactly when the intensification of porosity is observed. Notice that after initiation of fracture, the information of the process from the porosity field becomes less readable. It is due to the fact that the initial porosity is of the order  $6 \cdot 10^{-4}$ , while the fracture porosity is 0.36, making it impossible to obtain detailed information from the contour map where the quantities differ nearly four times.

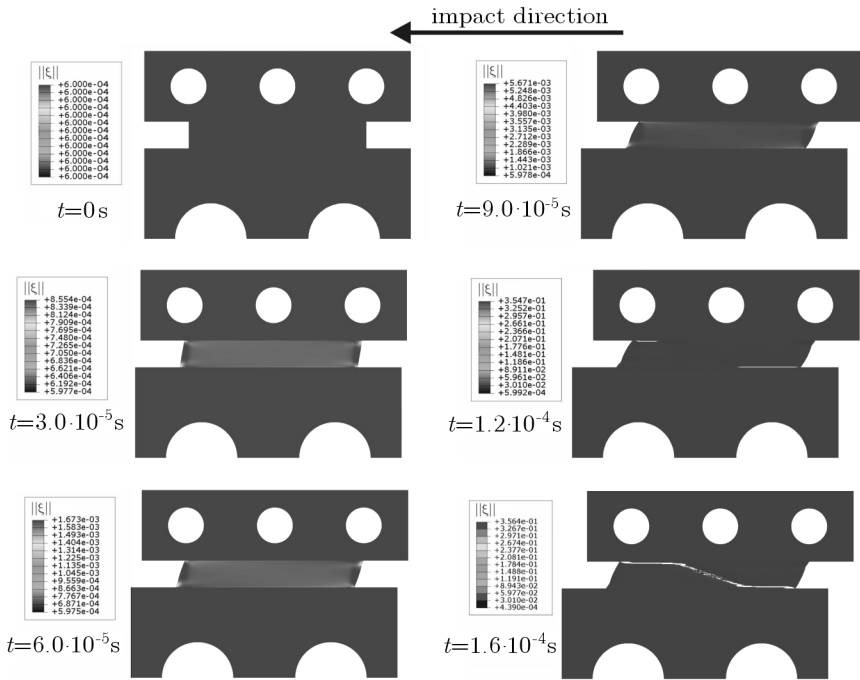


Fig. 12. Porosity evolution in Nowacki's specimen vs. time

Figure 13 presents directions of the intrinsic anisotropic microdamage process in time. For readability, only the information on directions in selected points are shown. The arrows map the principal directions of the microdamage tensor  $\xi$ . Due to physical interpretation given, the damage plane is the one perpendicular to the direction of maximal principal value presented by arrows in the plot. Notice that the orientation of softening directions changes through the specimen length showing that the problem is truly three dimensional (see also Fig. 14, where the isolines of displacement field in the direction of the specimen thickness are presented). Based on those principal directions, one can predict the possible damage plane shortly after the stabilisation of the process (after several viscoplastic wave reflections from boundaries), see Fig. 13 where the failure pattern is marked by the dotted line.

### 5. Conclusions

In the paper the numerical analysis of Nowacki's double shear test in the framework of the anisotropic thermo-elasto-viscoplastic model is presented. The novel is that computations cover not only elastic and viscoplastic ranges but,

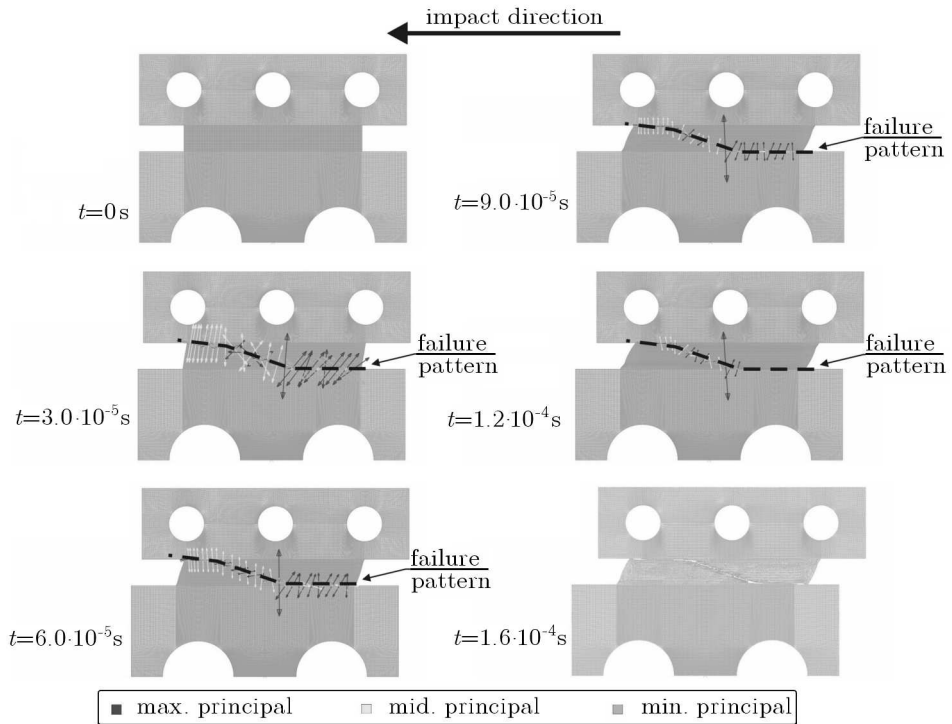


Fig. 13. Evolution of principal directions of the microdamage tensor through the damage zone in Nowacki's specimen vs. time

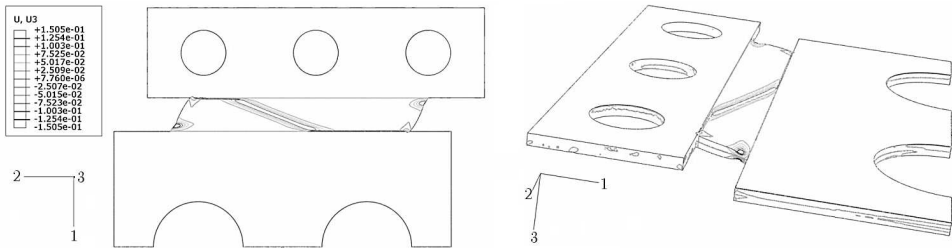


Fig. 14. Evolution of thickness in Nowacki's specimen vs. time

what is fundamental, the model describes the anisotropy of intrinsic microdamages, what enables one to obtain qualitatively and quantitatively new results compared with the existing models, namely: tracing the directions of softening and predict the damage path in time. It is crucial that the theory described gives a clear physical interpretation for all assumed variables in the model.

The performed analysis shows not only the possibilities of the recently developed constitutive technique, see Sumelka (2009) but, what is crucial, can

state a base for improving the discussed experimental technique, namely to answer the question on microdamage evolution in the process of time. This will help us to precise the definition of microdamage state, which influences the reliability of numerical analysis (Glema *et al.*, 2010). In the presented numerical calculations, the evolution equations are purely phenomenological. Nevertheless, the model is able to reproduce experimental observations with a very good agreement and gives a deep insight into the local thermomechanical process, what is crucial for the requirements of modern industry.

## References

1. *Abaqus Version 6.9ef1 Theory Manual*, 2010
2. ABU AL-RUB R.K., VOYIADJIS G.Z., 2006, A finite strain plastic-damage model for high velocity impact using combined viscosity and gradient localization limiters: Part I – theoretical formulation, *International Journal of Damage Mechanics*, **15**, 4, 293-334
3. CAMPBELL J.D., 1953, The dynamic yielding of mild steel, *Acta Metallurgica*, **1**, 6, 706-710
4. DIENES J.K., 1979, On the analysis of rotation and stress rate in deforming bodies, *Acta Mechanica*, **32**, 217-232
5. DORNOWSKI W., 1999, Influence of finite deformations on the growth mechanism of microvoids contained in structural metals, *Archives of Mechanics*, **51**, 1, 71-86
6. DORNOWSKI W., PERZYNA P., 2002a, Analysis of the influence of various effects on cycle fatigue damage in dynamic process, *Archive of Applied Mechanics*, **72**, 418-438
7. DORNOWSKI W., PERZYNA P., 2002b, Localized fracture phenomena in thermo-viscoplastic flow process under cyclic dynamic loadings, *Acta Mechanica*, **155**, 233-255
8. DORNOWSKI W., PERZYNA P., 2006, Numerical investigation of localized fracture phenomena in inelastic solids, *Foundations of Civil and Environmental Engineering*, **7**, 79-116
9. GARY G., NOWACKI W.K., 1994, Essai de cisaillement plan appliqué à des tôles minces, *Journal de Physique IV*, **4**, C8, 65-70
10. GLEMA A., 2004, *Analiza natury falowej zjawiska lokalizacji odkształceń plastycznych w ciałach stałych*, Publishing House of Poznan University of Technology, *Rozprawy*, **379** [in Polish]

11. GLEMA A., ŁODYGOWSKI T., PERZYNA P., 2008, Numerical investigation of dynamic shear bands in inelastic solids as a problem of mesomechanics, *Computational Mechanics*, **41**, 2, 219-229
12. GLEMA A., ŁODYGOWSKI T., PERZYNA P., SUMELKA W., 2006, Constitutive anisotropy induced by plastic strain localization, In: *35th Solid Mechanics Conference*, Kraków, Poland, September 4-8, 139-140
13. GLEMA A., ŁODYGOWSKI T., SUMELKA W., 2010, Towards the modelling of an anisotropic solids, *Computational Methods in Science and Technology*
14. GLEMA A., ŁODYGOWSKI T., SUMELKA W., PERZYNA P., 2009, The numerical analysis of the intrinsic anisotropic microdamage evolution in elasto-viscoplastic solids, *International Journal of Damage Mechanics*, **18**, 3, 205-231
15. GREBE H.A., PAK H.-R., MEYERS M.A., 1985, Adiabatic shear localization in titanium and Ti-6 pct Al-4 pct V alloy, *Metallurgical and Materials Transactions A*, **16**, 5, 761-775
16. KLEPACZKO J.R., 1990, Behavior of rock like materials at high strain rates in compression, *International Journal of Plasticity*, **6**, 415-432
17. KLEPACZKO J.R., 1994, An experimental technique for shear testing at high and very high strain rates. The case of mild steel, *International Journal of Impact Engineering*, **15**, 25-39
18. KLEPACZKO J.R., 2007, Constitutive relations in dynamic plasticity, pure metals and alloys, *Advances in Constitutive Relations Applied in Computer Codes*, CISM, Udine, Italy, July 23-27
19. KLEPACZKO J.R., NGUYEN H.V., NOWACKI W.K., 1999, Quasi-static and dynamic shearing of sheet metals, *European Journal of Mechanics – A/Solids*, **18**, 271-289
20. LEE E.H., 1969, Elastic-plastic deformation at finite strain, *ASME Journal of Applied Mechanics*, **36**, 1-6
21. ŁODYGOWSKI T., 1995, On avoiding of spurious mesh sensitivity in numerical analysis of plastic strain localization, *Computer Assisted Mechanics and Engineering Sciences*, **2**, 231-248
22. ŁODYGOWSKI T., 1996, *Theoretical and Numerical Aspects of Plastic Strain Localization*, Publishing House of Poznan University of Technology, **312**, D.Sc. Thesis
23. ŁODYGOWSKI T., GLEMA A., SUMELKA W., 2008, Anisotropy induced by evolution of microstructure in ductile material, In: *8th World Congress on Computational Mechanics (WCCM8)*, *5th European Congress on Computational Methods in Applied Sciences and Engineering (ECCOMAS 2008)*, Venice, Italy, June 30–July 5

24. ŁODYGOWSKI T., PERZYNA P., 1997a, Localized fracture of inelastic polycrystalline solids under dynamic loading process, *International Journal Damage Mechanics*, **6**, 364-407
25. ŁODYGOWSKI T., PERZYNA P., 1997b, Numerical modelling of localized fracture of inelastic solids in dynamic loading process, *International Journal for Numerical Methods in Engineering*, **40**, 4137-4158
26. ŁODYGOWSKI T., PERZYNA P., LENGNICK M., STEIN E., 1994, Viscoplastic numerical analysis of dynamic plastic shear localization for a ductile material, *Archives of Mechanics*, **46**, 4, 541-557
27. MARSDEN J.E., HUGHES T.J.H., 1983, *Mathematical Foundations of Elasticity*, Prentice-Hall, New Jersey
28. NARAYANASAMY R., PARTHASARATHI N.L., NARAYANAN C.S., 2009, Effect of microstructure on void nucleation and coalescence during forming of three different HSLA steel sheets under different stress conditions, *Materials and Design*, **30**, 1310-1324
29. NEMAT-NASSER S., GUO W.-G., 2003, Thermomechanical response of DH-65 steel plates over a wide range of strain rates and temperatures, *Mechanics of Materials*, **35**, 1023-1047
30. NEMES J.A., EFTIS J., 1991, Several features of a viscoplastic study of plate-impact spallation with multidimensional strain, *Computers and Structures*, **38**, 3, 317-328
31. NEMES J.A., EFTIS J., 1993, Constitutive modelling of the dynamic fracture of smooth tensile bars, *International Journal of Plasticity*, **9**, 2, 243-270
32. NOWACKI W.K., GADAJ P., LUCKNER J., 2006, Effect of strain rate on ductile fracture, Report IPPT, Warsaw, January
33. NOWAK Z., NOWACKI W.K., PERZYNA P., PEÇHERSKI R.B., 2007, Modelling of localized fracture phenomena in high strength steels, In: *10th European Mechanics of Materials Conference EMMC10*, Kazimierz Dolny, Poland, June 11-14
34. PERZYNA P., 1963, The constitutive equations for rate sensitive plastic materials, *Quarterly of Applied Mathematics*, **20**, 321-332
35. PERZYNA P., 1966, Fundamental problems in viscoplasticity, *Advances in Applied Mechanics*, **9**, 243-377
36. PERZYNA P., 1986a, Constitutive modelling for brittle dynamic fracture in dissipative solids, *Archives of Mechanics*, **38**, 725-738
37. PERZYNA P., 1986b, Internal state variable description of dynamic fracture of ductile solids, *International Journal of Solids and Structures*, **22**, 797-818
38. PERZYNA P., 1994, Instability phenomena and adiabatic shear band localization in thermoplastic flow process, *Acta Mechanica*, **106**, 173-205

39. PERZYNA P., 1995, Interactions of elastic-viscoplastic waves and localization phenomena in solids, In: *IUTAM Symposium on Nonlinear Waves in Solids*, Wegner J.L. and Norwood F.R. (Edit.), Victoria, Canada, August 15-20, 114-121
40. PERZYNA P., 2005, The thermodynamical theory of elasto-viscoplasticity, *Engineering Transactions*, **53**, 235-316
41. PERZYNA P., 2006, The thermodynamical theory of elasto-viscoplasticity accounting for microshear banding and induced anisotropy effects, In: *35th Solid Mechanics Conference*, Kraków, Poland, September 4-8, 35-36
42. PERZYNA P., 2008, The thermodynamical theory of elasto-viscoplasticity accounting for microshear banding and induced anisotropy effects, *Mechanics*, **27**, 1, 25-42
43. PEŁCHERSKI R.B., NOWACKI W.K., NOWAK Z., PERZYNA P., 2009, Effect of strain rate on ductile fracture. A new methodology, In: *Workshop, Dynamic Behaviour of Materials, In Memory of Our Friend and Colleague Prof. J.R. Klepaczko*, Metz, France, May 13-15, 65-73
44. RUSINEK A., KLEPACZKO J.R., 2009, Experiments on heat generated during plastic deformation and stored energy for TRIP steels, *Materials and Design*, **30**, 1, 35-48
45. SEAMAN L., CURRAN D.R., SHOCKEY D.A., 1976, Computational models for ductile and brittle fracture, *Journal of Applied Physics*, **47**, 11, 4814-4826
46. SHIMA S., OYANE M., 1976, Plasticity for porous solids, *International Journal of Mechanical Sciences*, **18**, 285-291
47. SUMELKA W., 2009, *The Constitutive Model of the Anisotropy Evolution for Metals with Microstructural Defects*, Publishing House of Poznan University of Technology, Poznań, Poland
48. SUMELKA W., GLEMA A., 2007, The evolution of microvoids in elastic solids, In: *17th International Conference on Computer Methods in Mechanics CMM-2007*, Łódź-Spała, Poland, June 19-22, 347-348
49. SUMELKA W., GLEMA A., 2009, Theoretical and computational aspects of implementation of anisotropic constitutive model for metals with microstructural defects, In: *18th Int. Conf. on Computer Methods in Mechanics CMM-2009*, Zielona Góra, Poland, May 18-21, 451-452
50. TRUESDELL C., NOLL W., 1965, *The Non-Linear Field Theories of Mechanics*, In: *Handbuch der Physik III/3*, Springer-Verlag, S. Flügge (Edit.)
51. VOYIADJIS G.Z., ABU AL-RUB R.K., 2006, A finite strain plastic-damage model for high velocity impacts using combined viscosity and gradient localization limiters: Part II – Numerical aspects and simulations, *International Journal of Damage Mechanics*, **15**, 4, 335-373

52. XIAO H., BRUHNS O.T., MEYERS A., 1997, Logarithmic strain, logarithmic spin and logarithmic rare, *Acta Mechanica*, **124**, 89-105

**Analiza testu podwójnego ścinania Nowackiego w ramach anizotropowego termo-sprężysto-lepkoplastycznego modelu materiału**

Streszczenie

W pracy przedstawiono numeryczne symulacje testu podwójnego ścinania, zaproponowanego przez prof. Nowackiego, w ramach sformułowania teorii lepkoplastyczności dla anizotropowych ciał stałych. Analizy numeryczne obejmują modele trójwymiarowe i są wykonane dla stali DH-36 w warunkach adiabatycznych (analiza ciał anizotropowych może być przeprowadzona wyłącznie na modelach trójwymiarowych). W trakcie analiz obserwuje się prędkości deformacji rzędu  $10^4$ - $10^7$  s<sup>-1</sup>, a czas trwania procesu do całkowitego zerwania próbki (utrata ciągłości w strefie lokalizacji) jest z przedziału 150-300  $\mu$ s. Oryginalność badań wynika z faktu uwzględnienia w definicji konstytutywnego modelu anizotropowego wewnętrznego procesu mikrouszkodzeń. W rezultacie, uzyskane wyniki dają jakościowo i ilościowo nowy obraz procesu, w szczególności umożliwiają śledzenie kierunków osłabienia oraz dokładniejsze (bliższe rezultatom eksperymentalnym) odwzorowanie ścieżki zniszczenia.

*Manuscript received April 21, 2010; accepted for print June 18, 2010*